Ballistic electron transmission through interfaces

M. D. Stiles and D. R. Hamann
AT&T Bell Laboratories, 600 Mountain Avenue, Murray Hill, New Jersey 07974-2070
(Received 18 December 1987)

We report on a new method for calculating ballistic electron transmission through epitaxial interfaces and its application to a silicon twist boundary. This method is based on constructing the electronic states of the infinite system from the generalized Bloch states for each layer in the structure; these states are matched together at the layer boundaries to construct the composite wave function. We find that the conduction-band electrons and the degenerate light and heavy holes within thermal energies of the band gap are strongly scattered by the twist boundary, but that the split-off holes in the same energy range are not. These results, which are unexpected from naive effective-mass considerations, can be simply understood in terms of flux patterns of the band-extrema wave functions on the interface-matching plane.

I. INTRODUCTION

The increasing ability to grow epitaxial interfaces[1] between semiconductors and between semiconductors and metals makes it important to understand how structurally perfect interfaces scatter electrons. For example, the possibility of using ballistic transport in multilayer structures to make high-speed transistors[2] requires an understanding of what happens to electrons at the interfaces of the proposed devices. We present a new approach, ideally suited to calculating transmission coefficients for interfaces, and demonstrate it by application to a silicon twist boundary.

This method is based on calculating the electronic states of the structures of interest, and using these states to calculate physical properties. Since the states of the actual infinite structures are calculated rather than those of supercells, the wave functions of the interface system contain the transmission and reflection coefficients directly. Besides these properties of scattering states, the energies and wave functions of interface states can be found using this method. The wave functions can be used to calculate matrix elements to describe processes like optical transitions. Problems that have been studied by other theoretical methods based on calculating the electronic wave functions of infinite systems include stacking-fault scattering in copper,[3] surface states,[4–9] heterojunctions,[10–14] negative electron-affinity photoemission,[15] and optical matrix elements.[16]

A silicon twist boundary in a (111) plane is the simplest system on which we could test the method and still get nontrivial results; in fact, the results we found were surprising, particularly from an effective-mass point of view. We found that near several band extrema the transmission across the twist boundary goes to zero. The simple explanation we found for this suggests that this should be a quite general result, and that such extrema might be identified from simple standard band calculations.

The method basically consists of constructing the generalized Bloch states in each material, and joining them together by matching them across the interfaces in the structure. The generalized Bloch states, which include both the usual propagating Bloch states and the evanescent states, are constructed in each layer by a variational basis-function approach leading to an eigenvalue problem for the boundary conditions of the states. The eigenvectors can be used to reconstruct the states. The states are matched through a self-consistent interface layer which allows the potential to vary smoothly from one material to the other. The matching is done using a constrained least-squares fit which preserves unitarity in the interface scattering matrix. For maximum generality, our application uses linearized augmented plane waves (LAPW's) as a basis set.

In Sec. II of this paper we discuss the general approach we have taken and its advantages, particularly in comparison to an interface Green-function approach. We illustrate our point with a one-dimensional example. The general method is presented in Sec. III, leaving specific application to the LAPW basis set to the Appendix. In Sec. IV we present the results of applying this method to electronic states of a silicon twist boundary. Finally, in Sec. V, we summarize the main points of this paper.

II. GENERAL DISCUSSION

There are straightforward ways to find the wave functions for a composite of two materials given either the Green functions[17] or the generalized Bloch states (including evanescent states) of both materials. If the potential permits an exact closed-form solution for the wave functions, the Green function can be constructed exactly and can be used to solve the composite problem. An example of such a potential is the pure muffin-tin potential upon which the layer Korringa-Kohn-Rostoker[18] (KKR) theory is based. For an arbitrary potential, there is no closed form for the wave functions, and a variational calculation in some basis is the only practical way to calculate them. Two possible ways to approach the composite problem are to use the variationally computed Bloch states in the spectral representation of the Green func-

tion,[19] or to use a different variational principle to compute the generalized Bloch states[20] from a basis set. In this section we discuss difficulties in using the spectral representation for an interface or surface problem, outline the variational form we use for the generalized Bloch states and the joining layer, and compare the approaches with a one-dimensional example.

Single-electron Green functions are used for finding solutions of Schrödinger equations with inhomogeneous terms. An interface system can be viewed as a special case of this in which the boundary values from one half-system are the inhomogeneous terms for the other half-system. In this case an interface Green function is constructed from the two half-systems through the bulk Green functions and their spatial derivatives evaluated at the matching plane. The bulk Green function satisfies an inhomogeneous defining equation such that operating on it by the Hamiltonian minus the energy gives a δ function of the two spatial arguments. For interface systems it is useful to integrate the defining equation by parts giving a result in terms of derivatives of the bulk Green function evaluated on the interface plane,

$$\lim_{z'\to 0^-}\left[\left.\frac{\partial G(E,\mathbf{r},\mathbf{r}')}{\partial z}\right|_{z=0}\right] - \lim_{z'\to 0^+}\left[\left.\frac{\partial G(E,\mathbf{r},\mathbf{r}')}{\partial z}\right|_{z=0}\right] = 2m\delta^{(2)}(\mathbf{R},\mathbf{R}') \ . \quad (1)$$

The position of the particle is denoted by $\mathbf{r}=(\mathbf{R},z)$, where the position parallel to the layer is given by $\mathbf{R}$ and the direction normal to the interface is the z direction.[21] (Throughout this paper we use the conventions that three-dimensional vectors are lower-case boldface Roman letters and two-dimensional vectors parallel to the interface plane are upper-case boldface Roman letters.) This discontinuity is used in solving for the interface Green function[17] in terms of the Green functions of the subsystems.

The bulk Green function can be constructed from its spectral representation by a sum over all propagating states in the bulk,

$$G(E,\mathbf{r},\mathbf{r}')=\lim_{\eta\to 0}\sum_n\int\frac{d^3k}{(2\pi)^3}\frac{e^{-i\mathbf{k}\cdot\mathbf{r}}u_n(\mathbf{k},\mathbf{r})^*u_n(\mathbf{k},\mathbf{r}')e^{i\mathbf{k}\cdot\mathbf{r}'}}{E-E_n(\mathbf{k})+i\eta} \quad (2)$$

where n is the band index, $\mathbf{k}$ is the wave vector, $u_n(\mathbf{k},\mathbf{r})$ is the periodic part of the Bloch state, and the $\mathbf{k}$ integral is over the Brillouin zone. In any numerical construction based on this equation, the sum over the energy bands needs to be truncated at some finite number and the integral over $\mathbf{k}$ needs to be approximated. With this truncation, the Green function no longer obeys the inhomogeneous defining equation; operating on the Green function by the Hamiltonian minus the energy gives a result that is everywhere finite. In particular, the discontinuity in the interface Green-function equation is zero within this approximation. The discontinuity will be zero in any approximation for the Green function that only includes any finite set of energy bands and is only reproduced in the limit that the number of bands kept in the spectral representation goes to infinity.[22]

The Green function calculated from its spectral representation is also susceptible to incorrect behavior at large distances from the interface if the integration over the wave vectors is not done sufficiently accurately. For a constant potential in one dimension, both of these features are illustrated in Fig. 1, in which we compare an exact decaying exponential with approximations generated by the spectral representation and by the variational construction method we describe below.

In using the spectral representation with a finite set of variational eigenfunctions, we are implicitly giving an expansion of the Green function which is analytic throughout space. The exact solution of the Schrödinger equation for a smooth potential is, of course, analytic. It is well known, however that piecewise analytic functions can often provide better approximations to unknown analytic functions. Examples are the spline fit,[23] and finite-element methods.[24] (LAPW basis functions themselves, in fact, are already only piecewise analytic because of their augmentation in muffin tins.[25])

In this spirit, we find that the best way to construct generalized Bloch states is one layer at a time. Our variational basis states with a given set of coefficients only represent a state in one layer; when we move to the next layer, we use a new set of coefficients. The coefficients can be chosen to preserve continuity in value and slope across each interface.

We use a bivariational formalism that includes double-sided boundary conditions in the variational functional for one layer to set up an eigenvalue problem for the

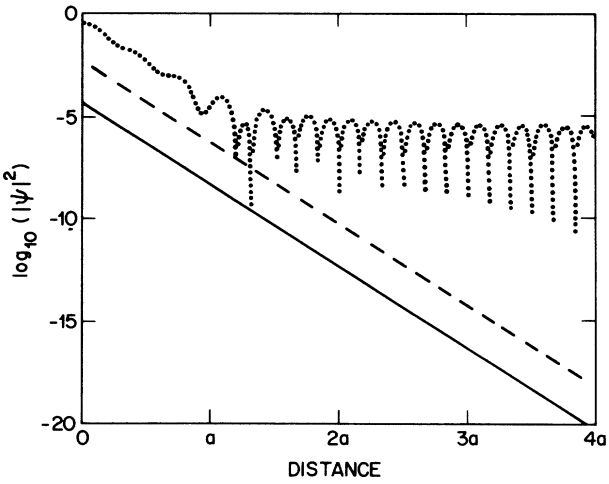

FIG. 1. A comparison of computational techniques for one-dimensional evanescent states. The solid curve is the exact decaying evanescent state at an energy (-8.23 eV) chosen to give a factor-of-100 decay over a distance ($a=5.92a_{\text{Bohr}}$) equal to the (111) layer thickness of silicon. The dotted curve is the state produced by a spectral representation of the free-particle Green function and the dashed curve is the state produced by the piecewise construction of the evanescent. The curves are shifted vertically for clarity; the solid and dashed lines are identical to within the thickness of the line.

states. This procedure is discussed in greater detail in the next section. In the one-dimensional example shown in Fig. 1, a piecewise approximation to an empty-lattice evanescent state is shown over several layers and compared with the exact results and the spectral representation. The piecewise approximation used six free-electron bands and two k points, giving a total of 12 states per layer, and for a consistent comparison the spectral representation used eight k points and six bands for all space. Note that the slope of the spectral representation curve is zero at the origin due to the truncation to a finite number of bands; the error at large distances is due to the finite k spacing for small values of k.

III. METHODS

To solve for the wave functions of a composite system, we calculate the generalized Bloch states of the layers that make up the semi-infinite bulk regions in the problem, using the minimum layer thickness consistent with the bulk periodicity. We then join them together either directly or through a self-consistent joining layer, whose potential we generate in a supercell calculation. In this section we outline this procedure, leaving the details of the application to a specific basis set, linearized augmented plane waves, to the Appendix.

Electronic-structure methods based on LAPW basis states have several advantages: they can be used with a general potential (no shape approximation), they can be used for any material, self-consistent potentials in suitable form are available from existing programs, and much of the calculation is independent of the energy at which the states are being calculated. We use LAPW eigenstates of these potentials for several wave vectors as the basis states to calculate the generalized Bloch states for each layer. Other methods that have been applied to semi-infinite interfaces include augmented plane waves (APW's),[3] empirical local pseudopotentials,[26] tight-binding models,[27,11] and the empirical Kane Hamiltonian.[28,12,10] Semi-infinite surfaces have been studied by related methods based on pseudopotentials,[5] an empirical potential APW method,[4] and a hybrid LAPW-KKR method.[29] The KKR method itself has been applied extensively to muffin-tin models of surfaces in computations of low-energy electron-diffraction intensities.[30]

The two approximations we make at this point are that the changes in the potential due to an interface are short ranged, and that the quasiparticle states which would correctly describe the transport in these systems can be approximated by local-density-functional eigenstates. The first approximation is quite reasonable, provided we include a self-consistently calculated interface layer when joining two very different materials. The second approximation is justified by the similarity between the quasiparticle states and the local-density-functional eigenstates.[31–33]

In the spirit of the preceding section, we calculate the generalized Bloch states by considering a layer which can be repeated periodically to construct the bulk crystal. The generalized Bloch states are constructed in this layer by a method similar to that used by Wachutka[4] using a basis-set expansion and a bivariational expression that treats both the Schrödinger equation and the layer boundary conditions variationally,[20]

$$J=\int_{\text{cell}} d^3r[\nabla\chi^*(\mathbf{r})\cdot\nabla\phi(\mathbf{r})+2m(V(\mathbf{r})-E)\chi^*(\mathbf{r})\phi(\mathbf{r})]-\int_F d\sigma[t^*(\mathbf{r})\phi(\mathbf{r})+\chi^*(\mathbf{r})t(\mathbf{r})]$$
$$+\tfrac{1}{2}\int_F d\sigma\{[\hat{\Lambda}\chi(\mathbf{r})]^*\phi(\mathbf{r})+\chi^*(\mathbf{r})[\hat{\Lambda}\phi(\mathbf{r})]\}\ . \tag{3}$$

The wave functions ϕ and χ are to be variationally computed, the volume integrals are over a cell defined by the faces F, the function t is the externally imposed boundary target value on the surface of the cell, F, $\hat{\Lambda}$, is an operator (by convention, the symbols for operators include a caret) on the wave function at the faces of the cell, and m is the electron mass.[21] For generalized Bloch states the cell over which the volume integrals are computed is a Wigner-Seitz cell, but cells that contain less than a unit supercell normal to the interface are also considered for joining bulk regions together. Throughout this paper we will differentiate between three terms: boundary values are the values and slopes (or some combination) of wave functions on the boundaries of a layer, target values are the inputs to a variational calculation that would be equaled by some boundary values in the limit that the solutions become exact, and boundary conditions are the restrictions, such as continuity, periodicity, or decay, that are applied to generate certain types of solutions.

For a layer, the wave function will be of the usual Bloch form parallel to the interface because the potential is periodic in that direction, in which case the contributions from the side boundaries of the cell will cancel. Since the Schrödinger equation is a second-order differential equation, two target values on one face of the layer (e.g., value and slope), or one on each face, fully determine the solution. For the variational calculation, targeting a linear combination of value and slope, on each face, yields the best stability and convergence properties.[4,20] The variational expression above, Eq. (3), uses a target value on each face given by

$$t_X(\mathbf{R})=\hat{\Lambda}\psi(\mathbf{R},z_X)+\hat{\partial}_n\psi(\mathbf{R},z_X)\ , \tag{4}$$

where $\psi(\mathbf{r})$ is the exact solution we are trying to find, ∂_n is symbolic for taking the derivative in the local surface-normal direction and X, denoting the interface surfaces, takes the values L, left, and R, right. The layer we are considering runs from z_L to z_R. $\hat{\Lambda}$ operates in either plane parallel to the interface, and is chosen to be

$$\hat{\Lambda}=\alpha\left[E_0-\frac{\partial^2}{\partial R^2}\right]^{1/2}\ , \tag{5}$$

with α and E_0 arbitrary constants.[4] $\hat{\Lambda}$ is used to treat

value and slope on equal footing in the boundary conditions. When the momentum parallel to the interface is large, $\hat{\Lambda}$ is large because the ratio of the normal slope to the value is expected to be large, as it is for free-space solutions.

The variational solution $\phi(\mathbf{r})$ will have boundary values

$$b_X(\mathbf{R})=\hat{\Lambda}\phi(\mathbf{R},z_X)+\hat{\partial}_n\phi(\mathbf{R},z_X) \tag{6}$$

that approximate the target values, $t_X(\mathbf{R})$. We will also need to consider the complementary set of boundary values,

$$c_X(\mathbf{R})=\hat{\Lambda}\phi(\mathbf{R},z_X)-\hat{\partial}_n\phi(\mathbf{R},z_X) . \tag{7}$$

Both b and c will enter when we construct wave functions throughout space by joining layers.

For our application, ϕ and χ are the same and the bivariational expression, Eq. (3), reduces to a variational expression. Furthermore, it can be expressed in a slightly more intuitive form,

$$\begin{aligned}J=&\tfrac{1}{2}\int_{\text{cell}}d^3r\{\phi^*(\mathbf{r})[2m(\hat{H}-E)\phi(\mathbf{r})]+[2m(\hat{H}-E)\phi(\mathbf{r})]^*\phi(\mathbf{r})\}\\&+\tfrac{1}{2}\sum_X\int_{\text{IWSC}}d^2R\{[(\hat{\Lambda}+\hat{\partial}_n)\phi(\mathbf{R},z_X)]^*\phi(\mathbf{R},z_X)+\phi^*(\mathbf{R},z_X)[(\hat{\Lambda}+\hat{\partial}_n)\phi(\mathbf{R},z_X)]\}\\&-\sum_X\int_{\text{IWSC}}d^2R[t_X^*(\mathbf{R})\phi(\mathbf{R},z_X)+\phi^*(\mathbf{R},z_X)t_X(\mathbf{R})] ,\end{aligned} \tag{8}$$

by integrating in by parts in such a way as to keep all of the terms explicitly Hermitian. The two-dimensional integrals are done over the interface Wigner-Seitz cell (IWSC). In general, the unsymmetrized Hamiltonian matrix is not Hermitian unless the basis states satisfy boundary conditions consistent with the integration volume being a closed system. The term "closed system" implies either infinite potential barriers, periodic boundary conditions, or an infinite system; none of these conditions apply in our application. By limiting the integration to a cell that is the product between a single-interface Wigner-Seitz cell and the layer width normal to the interface, we are required to consider only states with a given parallel wave vector. (Replacing the interface Wigner-Seitz cell by the entire layer would have enforced that constraint automatically.) The first term of Eq. (8) gives the variational requirement that the solution satisfy the Schrödinger equation in the interior of the cell, while the other two terms give the variational requirement that the boundary values equal the target values. In the second term, the boundary values, $b_X(\mathbf{R})$, have been written out explicitly to remind the reader that this term is quadratic in the solution, unlike the third term.

Given a target value and an energy we find the wave function in the layer for which the variational quantity is stationary. This wave function satisfies the Schrödinger equation in the layer and has the combination of boundary values given in Eq. (6) equal to the target value. From this wave function we can extract the complementary set of boundary values given in Eq. (7). By carrying out this procedure for a complete set of linearly independent target values, we can construct an operator that takes one set of boundary values (the b's) into another set (the c's). For matching purposes this operator contains all the essential information about the electronic states inside the layer. For the interface layer between the two bulk materials this is all the information necessary. For the bulk regions we need to apply the boundary conditions that the wave function not diverge at infinity. To apply these boundary conditions it is useful to construct the generalized Bloch states for the bulk regions. These states can be calculated from the boundary-value operator discussed above and the generalized Bloch condition discussed below.

We expand the solution ϕ in a basis set $\psi_i(\mathbf{r})$,

$$\phi(\mathbf{r})=\sum_i a_i\psi_i(\mathbf{r}) . \tag{9}$$

In general, the basis set could be arbitrary functions consistent with parallel Bloch periodicity. In our work, the index i includes a three-dimensional Bloch wave-vector index and a band index. Using the LAPW eigenstates as bases rather than the LAPW's themselves has the advantage that the basis can be truncated in a way that leaves the important band states well converged. In terms of the basis set, we compute the overlap matrix,

$$O_{ij}=\int_{\text{cell}}d^3r\,\psi_i^*(\mathbf{r})\psi_j(\mathbf{r}) , \tag{10}$$

the Hamiltonian matrix

$$H_{ij}=\tfrac{1}{2}\int_{\text{cell}}d^3r\{\psi_i^*(\mathbf{r})[\hat{H}\psi_j(\mathbf{r})]+[\hat{H}\psi_i(\mathbf{r})]^*\psi_j(\mathbf{r})\} , \tag{11}$$

and a boundary-term matrix,

$$\begin{aligned}B_{ij}=\tfrac{1}{2}\sum_X\int_{\text{IWSC}}d^2R\{&[(\hat{\Lambda}+\hat{\partial}_n)\psi_i(\mathbf{R},z_X)]^*\psi_j(\mathbf{R},z_X)\\&+\psi_i^*(\mathbf{R},z_X)[(\hat{\Lambda}+\hat{\partial}_n)\psi_j(\mathbf{R},z_X)]\} .\end{aligned} \tag{12}$$

To construct these matrices we need some quantities that are not used in the usual LAPW method—we need the

overlap and Hamiltonian matrix elements over a single cell between states with $\Delta k_z \neq 0$, and we need the value and slope of the wave functions on the endplanes. In the Appendix we describe how these are calculated.

To find the states that minimize the functional J, we define an inverse Green matrix

$$G_{ij}^{-1}(E)=2mH_{ij}+B_{ij}-2mEO_{ij} , \tag{13}$$

which differs from the usual definition of the Green matrix by the inclusion of the boundary matrix. We expand the boundary values of the basis states and the target values in interface reciprocal-lattice vectors,

$$\psi_i(\mathbf{R},z_X)=e^{i\mathbf{K}\cdot\mathbf{R}}\frac{1}{\Omega^{1/2}}\sum_{\mathbf{G}} e^{i\mathbf{G}\cdot\mathbf{R}}\psi_{i,X,\mathbf{G}} , \tag{14}$$

$$t_X(\mathbf{R})=e^{i\mathbf{K}\cdot\mathbf{R}}\frac{1}{\Omega^{1/2}}\sum_{\mathbf{G}} e^{i\mathbf{G}\cdot\mathbf{R}}t_{X,\mathbf{G}} . \tag{15}$$

The normalization of the states, $\Omega^{-1/2}$, where Ω is the volume of the Wigner-Seitz cell, has been factored out of the reciprocal-lattice expansion of the states. Combining all of these expressions gives a matrix variational expression

$$J=\sum_i\sum_j a_i^* G_{ij}^{-1}(E)a_j - \frac{A}{\Omega}\sum_j\sum_X\sum_{\mathbf{G}}(t_{X,\mathbf{G}}^*\psi_{j,X,\mathbf{G}}a_j+a_j^*\psi_{j,X,\mathbf{G}}^* t_{X,\mathbf{G}}) , \tag{16}$$

where A is the area of the interface Wigner-Seitz cell. Minimizing this with respect to a_i^* gives a set of inhomogeneous linear equations for the basis-function expansion coefficients of the variational state with the external target values $t_{X,\mathbf{G}}$. With the expansion coefficients, the variational wave function can be calculated and both sets of boundary values mentioned above, the $b_{X\mathbf{G}}$'s and $c_{X\mathbf{G}}$'s, can be computed from the value and slope of the basis functions on the endplanes. These boundary values can be expressed as matrices operating on the original target values,

$$c_{X,\mathbf{G}}=\sum_{X'}\sum_{\mathbf{G}'} S_{X,\mathbf{G},X',\mathbf{G}'}t_{X',\mathbf{G}'} , \tag{17}$$

$$b_{X,\mathbf{G}}=\sum_{X'}\sum_{\mathbf{G}'} T_{X,\mathbf{G},X',\mathbf{G}'}t_{X',\mathbf{G}'} , \tag{18}$$

where

$$S_{X,\mathbf{G},X',\mathbf{G}'}=\sum_i\sum_j[(\Lambda_{\mathbf{G}}\psi_{i,X,\mathbf{G}}-\hat{\partial}_n\psi_{i,X,\mathbf{G}})]\times[G_{ij}(E)]\left[\frac{A}{\Omega}\psi_{j,X',\mathbf{G}'}^*\right] , \tag{19}$$

$$T_{X,\mathbf{G},X',\mathbf{G}'}=\sum_i\sum_j[(\Lambda_{\mathbf{G}}\psi_{i,X,\mathbf{G}}+\hat{\partial}_n\psi_{i,X,\mathbf{G}})]\times[G_{ij}(E)]\left[\frac{A}{\Omega}\psi_{j,X',\mathbf{G}'}^*\right] . \tag{20}$$

If the calculation could be done with a complete basis set, $T_{X,\mathbf{G},X',\mathbf{G}'}$ would be a unit matrix; Wachutka[4] implicitly treats it as such by equating $t_{X\mathbf{G}}$ and $b_{X\mathbf{G}}$. In our formulation of the layer problem, the input target values and the output boundary values are of the same form, both sides are treated equally, and the value and slope are treated on the same footing.

In the above discussion, we have treated the target values as given. In practice, we do not know what sets of $t_{X,\mathbf{G}}$'s will yield the physical states we want. This must be determined once all the layers in the problem are joined together as with spline fits.[23] Equations (17) and (18) can be regarded as providing $4N_{\mathbf{G}}$ constraints among $6N_{\mathbf{G}}$ unknowns $t_{X,\mathbf{G}}$, $b_{X,\mathbf{G}}$, and $c_{X,\mathbf{G}}$. The remaining constraints are supplied by the boundary conditions, value and slope matching across the interfaces of the joined layers.

Matching through bulk regions, where all layers are identical, can be systematized in terms of generalized Bloch functions, introducing the physical boundary conditions of asymptotic behavior at $\pm\infty$. These functions satisfy

$$\phi(\mathbf{R},z_R)=e^{-i(k_z+i\kappa)(z_L-z_R)}e^{-i\mathbf{K}\cdot\mathbf{R}_0}\phi(\mathbf{R}+\mathbf{R}_0,z_L) , \tag{21}$$

where $k_z+i\kappa$ is the unknown complex wave vector normal to the interface, $\mathbf{K}$ is the (conserved) wave vector parallel to the interface, and $\mathbf{R}_0$ is a parallel translation such that $\mathbf{R}_0+\hat{\mathbf{z}}(z_L-z_R)$ is a lattice vector of the bulk material. For the bulk regions, the cell over which the volume integrals are done in Eq. (8) is a Wigner-Seitz cell, and the potential between z_L and z_R can be repeated periodically to generate the bulk potential. We obtain from Eq. (21) an additional $2N_{\mathbf{G}}$ equations for the boundary values, which can be written

$$b_{R,\mathbf{G}}=e^{-i(k_z+i\kappa)(z_L-z_R)}e^{i\mathbf{G}\cdot\mathbf{R}_0}c_{L,\mathbf{G}} , \tag{22}$$

$$c_{R,\mathbf{G}}=e^{-i(k_z+i\kappa)(z_L-z_R)}e^{i\mathbf{G}\cdot\mathbf{R}_0}b_{L,\mathbf{G}} . \tag{23}$$

There are now $6N_{\mathbf{G}}$ homogeneous equations in $6N_{\mathbf{G}}+1$ unknowns where the additional unknown is the complex wave vector. Equations (17), (18), (22), and (23) can be manipulated into the form of a generalized complex linear eigenvalue problem,

$$\begin{bmatrix}\mathbf{S}_{R,\mathbf{G},R,\mathbf{G}'} & \mathbf{S}_{R,\mathbf{G},L,\mathbf{G}'}\\ \mathbf{T}_{R,\mathbf{G},R,\mathbf{G}'} & \mathbf{T}_{R,\mathbf{G},L,\mathbf{G}'}\end{bmatrix}\begin{bmatrix}\mathbf{t}_{R,\mathbf{G}'}\\ \mathbf{t}_{L,\mathbf{G}'}\end{bmatrix}=\lambda\begin{bmatrix}\delta_{\mathbf{G},\mathbf{G}''}e^{i\mathbf{G}\cdot\mathbf{R}_0} & 0\\ 0 & \delta_{\mathbf{G},\mathbf{G}''}e^{i\mathbf{G}\cdot\mathbf{R}_0}\end{bmatrix}\begin{bmatrix}\mathbf{T}_{L,\mathbf{G}'',R,\mathbf{G}'} & \mathbf{T}_{L,\mathbf{G}'',L,\mathbf{G}'}\\ \mathbf{S}_{L,\mathbf{G}'',R,\mathbf{G}'} & \mathbf{S}_{L,\mathbf{G}'',L,\mathbf{G}'}\end{bmatrix}\begin{bmatrix}\mathbf{t}_{R,\mathbf{G}'}\\ \mathbf{t}_{L,\mathbf{G}'}\end{bmatrix} , \tag{24}$$

where $\lambda=e^{-i(k_z+i\kappa)(z_L-z_R)}$. Straightforward algorithms exist for solving such eigenvalue problems.[34] The eigenvectors from this equation can be used to reconstruct the generalized Bloch states in the layer in question, and the boundary values for these states. The boundary values can be used, in turn, to compute the flux carried by each of the states through the layer boundaries. Since these states are stationary solutions of a Schrödinger equation,

the net flux through any plane is the same as it is for any parallel plane, particularly a plane infinitely far from the interface. Generalized Bloch states that decay in either direction do not carry any net current for this reason.

The complex wave vectors as a function of the electron energy make up the complex band structure.[35,36] Advantages of the method we have described over other methods that have been used to calculate complex band structures are that it gives all the eigenvalues at a particular energy in one calculation, it only gives each eigenvalue once, and the matrices used depend on energy only explicitly through the matrix inversion of Eq. (13) to get the Green function used in Eqs. (19) and (20). Since the eigenvalue problem is based on the boundary conditions, it gives the appropriate number of eigenstates needed to join a set of bulk layers to other layers.

In contrast, complex band-structure methods based on searching for complex wave vectors that yield real energies give just one state at a time.[3] APW- and KKR-based methods have additional implicit nonlinear energy dependencies in the matrices for boundary-based eigenvalue problems. Finally, plane-wave-specific methods[26] (defined for local pseudopotentials only) give many redundant eigenvectors which must be sorted in some way to identify the correct subset.

To solve for the electronic states of an interface between two semi-infinite materials, we first calculate all of the generalized Bloch states for each of the materials. These states enable us to translate the physical boundary conditions we understand (incident, transmitted, and reflected propagating states far from the interface) into detailed numerical boundary conditions at the interface. Then we calculate the S matrix and T matrix defined in Eqs. (19) and (20) for a joining layer. In particular, we use a part of a supercell between a plane on which the potential is essentially that of the bulk on the left, and a plane on which the potential is essentially that of the bulk on the right. It is useful to use such joining layers because they minimize the spurious reflection and transmission due to the large discontinuities in the potential that occur in general when two bulk potentials are joined together. In principle, to have no potential discontinuity, an arbitrarily large supercell is required, but, in practice, the potentials are screened so rapidly that just a few layers is enough to do a good job.

To match the interfacial wave functions we divide space into three regions, the bulk region A extending toward infinity to the left, bulk region B extending toward infinity to the right, and the center region C. In each of the bulk regions, we find the possible incident states from the set of generalized Bloch states computed in Eq. (24); these are states that are propagating toward the interface and are labeled with the superscript "in." The outgoing states in each bulk are both the generalized Bloch states that propagate away from the interface, and the evanescent states that decay away from the interface. There is an outgoing state in each bulk region for each interfacial reciprocal-lattice vector included in the description of the states. For a state incoming from the left, the full state in region A is expanded in terms of the generalized Bloch states with arbitrary coefficients for the outgoing states,

$$\phi^A(\mathbf{r})=\phi_i^{A\,\mathrm{in}}(\mathbf{r})+\sum_j x_j^A \phi_j^{A\,\mathrm{out}}(\mathbf{r}) \ . \tag{25}$$

There is a similar expansion for the state in region B without an incoming state, and there are a total of $2N_G$ boundary values to be matched.

The S matrix in the center region relates all the boundary values on the center region to each other. The boundary values on the center region are related to the boundary values on the bulks to either side by the transformations $L \rightarrow R$ and $b \rightarrow c$ because of the change in direction of the interface normal. The result is a set of equations for the coefficients of the outgoing states, $\mathbf{x}$, in terms of the boundary values of the incoming eigenstate, $\mathbf{b}^{\mathrm{in}}$ and $\mathbf{c}^{\mathrm{in}}$, the boundary values of the outgoing eigenstates, $\mathbf{b}^{\mathrm{out}}$ and $\mathbf{c}^{\mathrm{out}}$, and the renormalized S matrix of the joining layer, $\tilde{\mathbf{S}}^C$,

$$\mathbf{AX}=\mathbf{B} \ , \tag{26}$$

where

$$\mathbf{X}=\begin{bmatrix}\mathbf{x}^A\\ \mathbf{x}^B\end{bmatrix} \ , \tag{27}$$

$$\mathbf{A}=\begin{bmatrix}\tilde{\mathbf{S}}_{LL}^C\mathbf{c}_R^{A\,\mathrm{out}}-\mathbf{b}_R^{A\,\mathrm{out}} & \tilde{\mathbf{S}}_{LR}^C\mathbf{c}_L^{B\,\mathrm{out}}\\ \tilde{\mathbf{S}}_{RL}^C\mathbf{c}_R^{A\,\mathrm{out}} & \tilde{\mathbf{S}}_{RR}^C\mathbf{c}_L^{B\,\mathrm{out}}-\mathbf{b}_L^{B\,\mathrm{out}}\end{bmatrix} \ , \tag{28}$$

$$\mathbf{B}=-\begin{bmatrix}\tilde{\mathbf{S}}_{LL}^C\mathbf{c}_R^{A\,\mathrm{in}}-\mathbf{b}_R^{A\,\mathrm{in}}\\ \tilde{\mathbf{S}}_{RL}^C\mathbf{c}_R^{A\,\mathrm{in}}\end{bmatrix} \ . \tag{29}$$

The renormalized S matrix, $\tilde{\mathbf{S}}^C$, is the matrix relating the boundary values, $b_{X,\mathrm{G}}$ and $c_{X,\mathrm{G}}$, to each other in region C given by

$$\tilde{\mathbf{S}}=\mathbf{S}\mathbf{T}^{-1} \ . \tag{30}$$

The dimensions of the matrix $\mathbf{A}$ are $2N_G \times N^{\mathrm{out}}$, $\mathbf{X}$ is an N^{out} element vector, and $\mathbf{B}$ a $2N_G$ element vector. Similar equations are satisfied if the incident state is from the right in the material B; the inhomogeneous term $\mathbf{B}$ changes to resemble the right half of matrix $\mathbf{A}$ with the "out" matrices replaced by the "in" vectors. Our procedures give exactly N_G outgoing generalized Bloch states for each material, so, in principle, the set of linear inhomogeneous equations represented by Eq. (25) has one unique solution. In practice, as discussed below, some of our variational evanescent states are not well converged. They may have nonzero current densities on the matching plane, or other unphysical characteristics. If we discard these states, it is necessary to solve these equations in a least-squares sense as there are more equations than unknowns.

In fact, we find it useful to solve this set of equations in a least-squares sense with an additional constraint. It is best to force the error out of the quantities of principle interest, provided it is possible to estimate the error involved. In particular, we impose a unitarity constraint; the total outgoing flux must equal the incoming flux. This leads to some mismatch in the value and slope at the interface because of the unconverged evanescent states. We can quantify the mismatch by the residual of the least-squares matching, and we have found that enforcing

the constraint makes very small contributions. To set up the system of constrained equations we minimize the squared matching error minus a Lagrange multiplier γ times the flux error,

$$(\mathbf{AX}-\mathbf{B})^{\dagger}\mathbf{W}(\mathbf{AX}-\mathbf{B})-\gamma(\mathbf{X}^{\dagger}\mathbf{FX}-f_0)\ , \tag{31}$$

where $\mathbf{W}$ is a diagonal weighting matrix for the interface reciprocal-lattice vectors, f_0 is the incoming flux, and $\mathbf{F}$ is a diagonal matrix of the flux in each of the outgoing propagating states. In this calculation we use the identity matrix for $\mathbf{W}$, but we expect that in less-well-converged calculations it will be useful to deemphasize the large $\mathbf{G}$ contributions to the matching. Varying Eq. (31) with respect to $\mathbf{X}^{\dagger}$ gives

$$\mathbf{A}^{\dagger}\mathbf{WAX}-\gamma\mathbf{FX}=\mathbf{A}^{\dagger}\mathbf{WB}\ , \tag{32}$$

which, with the flux constraint, gives $N^{\text{out}}+1$ equations in the unknowns $\gamma,\mathbf{X}$. Unfortunately, these are no longer linear equations, and they cannot be solved by conventional methods. We have developed an iterative method to solve them, which converges whenever the constraint is not violated too badly by the unconstrained $\gamma=0$ solution. This condition is certainly achieved for any reasonably complete wave-function basis set.

Our iterative procedure is motivated as follows. Suppose we have a good approximation $\gamma^{n-1},\mathbf{X}^{n-1}$ to the solution of Eq (32). With algebraic manipulation, we find

$$(\mathbf{A}^{\dagger}\mathbf{WA}-\gamma^{n-1}\mathbf{F})\mathbf{X}=\mathbf{A}^{\dagger}\mathbf{WB}+(\gamma-\gamma^{n-1})\mathbf{FX}^{n-1}+(\gamma-\gamma^{n-1})\mathbf{F}(\mathbf{X}-\mathbf{X}^{n-1})\ . \tag{33}$$

The right-hand side has terms of order 0, 1, and 2 in the error of the approximate solution. We drop the term of order 2 and regard the remainder as an equation determining an improved approximation $\gamma^{n},\mathbf{X}^{n}$. Solving the two inhomogeneous linear equations

$$(\mathbf{A}^{\dagger}\mathbf{WA}-\gamma^{n-1}\mathbf{F})\mathbf{X}_0^{n}=\mathbf{A}^{\dagger}\mathbf{WB} \tag{34}$$

and

$$(\mathbf{A}^{\dagger}\mathbf{WA}-\gamma^{n-1}\mathbf{F})\mathbf{Y}^{n}=\mathbf{FX}^{n-1}\ , \tag{35}$$

enables us to express $\mathbf{X}^{n}$ as

$$\mathbf{X}^{n}=\mathbf{X}_0^{n}+(\gamma^{n}-\gamma^{n-1})\mathbf{Y}^{n}\ , \tag{36}$$

where γ^{n} is to be determined. Substituting Eq. (36) in the flux-conservation constraint, we find terms of order 0, 1, and 2 in $\gamma^{n}-\gamma^{n-1}$. Dropping the second-order terms as above yields

$$\gamma^{n}=\gamma^{n-1}+\frac{\mathbf{X}_0^{n\dagger}\mathbf{FX}_0^{n}-f_0}{\mathbf{X}_0^{n\dagger}\mathbf{FY}^{n}+\mathbf{Y}^{n\dagger}\mathbf{FX}_0^{n}}\ . \tag{37}$$

We start the iteration with $\gamma^{0}=0$, find $\mathbf{X}_0^{1}$ from Eq. (34), and use $\mathbf{X}^{0}=\mathbf{X}_0^{1}$ in Eq. (35).

Having computed the amplitudes of the generalized Bloch states, x_j^{A} and x_j^{B}, we compute the transmission coefficient by an incoherent sum of the fluxes carried by each of the propagating generalized Bloch states

$$T=\frac{1}{f_0}\sum_j |x_j^{B}|^2 f_j^{B}\ , \tag{38}$$

where f_j^{B} is the flux in each of the transmitted states. There is a similar expression for the reflection coefficient in terms of amplitudes and fluxes in the other bulk region of space.

Most interface or surface problems have been solved using simple matching of value and slope, but two other approaches have been used. One (which is based on generalized Bloch states found by a search rather than a variational calculation) uses a variational calculation of the scattering-theory S matrix to compute the transmission and reflection coefficients.[3] Given variationally calculated states, however, this method entails far more work than is required. An alternative method, the assembly of boundary-controlled monolayers (ABCM's),[4] is based on layer doubling, extending the intermediate region far enough so that it is only necessary to use the propagating outgoing states in the matching. This method does not explicitly control the amplitudes of any evanescent states, so it is not clear how errors related to poorly converged evanescents affect the results.

There are technical differences between our calculation of the generalized Bloch functions and that of Wachutka[4] that affect how these wave functions are joined to make a composite wave function. These differences are related to the difference between the target values, $\mathbf{t}$, and the boundary values, $\mathbf{b}$, and the difference between the matrix that relates these two quantities, $\mathbf{T}$, and the unit matrix. If $\mathbf{t}$ and $\mathbf{b}$ are taken to be the same, the resulting wave functions have discontinuous values and slopes across the interface between two layers, but are the best variational approximation in each layer to the exact solution. If they are not taken to be the same, which entails using the matrix $\mathbf{T}$, the resulting wave functions are constrained to have continuous values and slopes, but are not as good approximations to the exact solution within each layer because there is less variational freedom in the layer when the constraint is included. Neither of these approaches produces the absolute best variational approximation to the wave function over several layers. That solution would have continuous value, since a discontinuity would contribute an infinite energy, but would have a discontinuous slope at the layer boundaries, because such a discontinuity only has a finite energy cost, and the additional variational freedom would allow a better solution over the whole range. Finding this best variational solution is a much more difficult calculation because all layers must be treated together.

We have carried out numerical calculations for a one-dimensional free particle and for bulk silicon both using the numerically calculated $\mathbf{T}$, and replacing it by its fully converged form, a unit matrix. For the silicon calculations reported here, $\mathbf{T}$ is very close to a unit matrix, the average absolute value of an off-diagonal component being less than 10^{-3} and the average absolute deviation of the diagonal elements from 1 was less than 10^{-2}. As anticipated above, the unit-matrix approximation gives more accurate decay constants for a given basis size, at the hidden cost of infinite interlayer energies.

Our approach can be generalized from single interfaces to complex structures, such as multiple quantum wells in compound semiconductor superlattices, which are often

too large to treat by direct supercell methods. Using the coefficients of appropriate generalized Bloch functions in each inequivalent bulklike layer as variables, the matching error at all interfaces can be minimized simultaneously. For sufficiently thick bulk regions, we can simply assemble our single-interface results for the scattering matrices of the propagating states.

Finally we note that for energies in the band gap of both materials, there are no propagating states and the matching equation, Eq. (24), becomes homogeneous. Solutions exist only at special energies where the determinant of **A** vanishes. For least-squares matching with a subset of evanescents, these energies correspond to sharp minima in the matching residual.

IV. RESULTS

A. Si complex band structure

In the preceding section we describe how we calculate the generalized Bloch states for a particular material; in Figs. 2 and 3 we show a subset of the complex wave vectors for such states in silicon, those in ⟨111⟩ directions relevant for a (111) interface. Such plots are called complex band-structure plots in analogy to the usual band-structure plots. In general, there are an infinite number

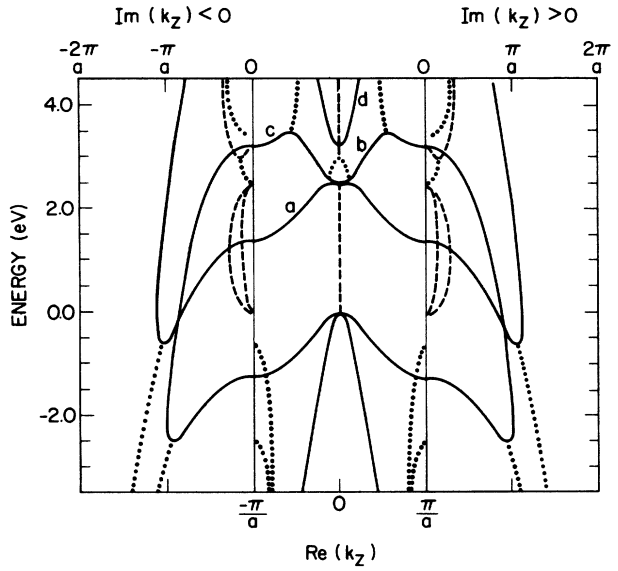

FIG. 2. The complex band structure of silicon in the [111] direction through Γ. The solid lines in the center panel show the dispersion of the propagating Bloch states. The solid lines in the outer two panels show the imaginary part of the wave vector (decay constant) for those generalized Bloch states with a real part at the zone boundary. The dashed curves in the outer panels show the imaginary parts of those generalized Bloch states with a zero real part, and the dashed curves in the middle panel show that real part. The dotted curves in the middle and outer panels show the real and imaginary parts, respectively, of the wave vectors that have a general real part. For clarity only the wave vectors having the smallest imaginary parts are shown. The labels for the lowest conduction bands (propagating states) are referred to in Fig. 5.

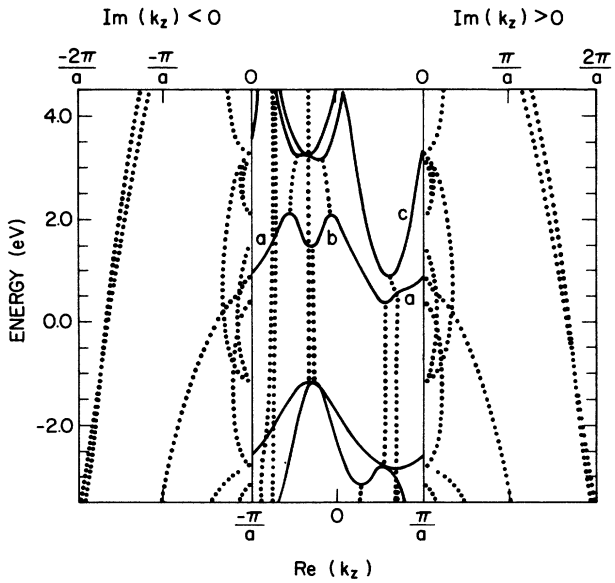

FIG. 3. The complex band structure of silicon in the [111] direction through the conduction-band minimum. The solid lines in the center panel show the dispersion of the propagating Bloch states. The dotted curves in the middle and outer panels show the real and imaginary parts, respectively, of the wave vectors for the generalized Bloch states. For clarity, only the wave vectors having the smallest imaginary parts are shown. The labels for the lowest conduction bands (propagating states) are referred to in Fig. 6.

of such states at any energy, but we only calculate a finite subset and show only those whose wave vectors have the smallest decay constants.

The real parts of the wave vectors are plotted in the center panel of each figure and the imaginary parts that are greater than and less than zero are plotted in the right- and left-hand panels, respectively. We rely on the reader to be able to identify which real part goes with which imaginary part, bearing in mind that states evolve continuously with increasing energy and states with complex wave vectors are always paired. When the imaginary parts of a pair of evanescents go to zero, the real part of the wave vector splits and becomes two propagating states; at band maxima two propagating states merge and become a pair of evanescent states.

Figure 2 shows the complex band structure along the Λ line in the Brillouin zone; these states have a parallel wave vector equal to zero. Two consequences of the Λ line being a symmetry line of the silicon Brillouin zone are that many of the states are degenerate and most of the complex wave vectors have real parts either at the zone center or the zone boundary. In this calculation we have neglected spin-orbit coupling so that the light-hole and heavy-hole bands are degenerate along the entire Λ line in Fig. 2, and the split-off hole band is degenerate with the other two at the zone center Γ.

Figure 3 shows the complex band structure in the [111] direction passing through the minimum in the conduction band, which is 0.85 of the way toward the X point along the Δ line. There are two values of the real part of

the perpendicular wave vector that intersect symmetry lines of the Brillouin zone, but the rest of the points are at general points in Brillouin zone. Due to the lack of symmetry, the real parts of the complex wave vectors have general values and none of the states are degenerate.

Sufficiently near band extrema, the energies of states are quadratic functions of the wave vector (ignoring spin-orbit coupling). The effective-mass approximation uses the curvature of the dispersion to predict the decay constants of the evanescent states. This works well close enough to the band extrema, but eventually breaks down; particularly in midgap regions the decay constants are not well described by the quadratic form from either extremum. A particularly interesting case where the effective-mass approximation has a very limited range of validity is in the region near the conduction-band minimum. An examination of the states' wave functions shows that those near this minimum are similar to those in the next-higher band, but not to those in the conduction band at energies above the "glitch" where there is a rapid change in the slope of the band. This behavior is consistent with an interpretation of these bands as an avoided crossing between a free-electron-like parabola with a small mass and one with a larger mass and a slightly higher minimum displaced toward higher k_z. This interpretation also explains the behavior of the evanescent state coupled to the next-higher band. At energies well below the conduction-band minimum, it behaves as if it were coupled to the larger-mass free-electron-like parabola. At the curve crossing, it veers toward the actual minimum it is coupled to. In a matching problem, treating these two bands in an effective-mass approximation would give unreliable results.

An advantage of using a complex band-structure method based on an existing real band-structure procedure is that the band structure calculated by the existing method can be used to test the convergence of the complex band structure by comparing the propagating states. To carry out this test, we fitted the LAPW bands with a cubic spline, and computed interpolated LAPW energies for each of the real wave vectors found using the complex band-structure program. For the split-off hole valence band in Fig. 2, the root-mean-square error between the complex band-structure and the LAPW energies was 10 meV, for the light- and heavy-hole bands it was 5 meV, and for the conduction band in Fig. 3 it was 3 meV.

Most of the states computed for the complex band structure are not as accurate as the propagating states discussed above. These states and the evanescent states that also have a small mean planar kinetic energy are well represented, but states with mean planar kinetic energies comparable to the cutoff are not. In a conventional LAPW calculation of real bands, states that have a kinetic energy comparable to the cutoff are not well converged, but they lie above the other states in energy so they can be easily sorted out. In the complex band structure the poorly converged states are not separated by having a larger decay constant normal to the interface. A guide to the convergence of a state is the proximity of its mean planar kinetic energy to the cutoff.

Another indication of a poorly converged state is the current of that state on the boundary planes, since evanescent states which are exact solutions of a time-independent Schrödinger equation have zero net current. The current in the poorly converged states is not a time-independent current that propagates to infinity away from the interface, but rather it is a consequence of the actual time dependence of the approximate description of the state and decreases as the amplitude of the state decreases. The current density of a poorly converged state is most usefully discussed in terms of a flux ratio, the ratio of the normal current density integrated over the boundary plane to the probability density integrated over the boundary plane; for a propagating state away from a band extremum this number is typically of order 1 in atomic units $(m_e a_0)^{-1}$. States with different parallel wave vectors behave differently depending on the symmetry of the basis set; the states in Fig. 2 have a special parallel wave vector, and a symmetric basis set and the states in Fig. 3 have a general parallel wave vector and an asymmetric basis set. Most of the states calculated with the symmetric basis set as in Fig. 2 have a flux ratio of less than 10^{-6}; some of these are well converged and others are not. For these states the term "well converged" is not well defined operationally, but those that are not well converged have decay constants that are smaller than they should be. A subset of the well-converged states with the smallest planar kinetic energies are shown in Fig. 2. There are other states with this parallel wave vector that have flux ratios of up to 0.015; these states are clearly not well converged and have large mean planar kinetic energies. The states shown in Fig. 3 (a well-converged subset of the states calculated at that parallel wave vector) all have flux ratios of less than 0.001 and have small mean planar kinetic energies. The other states with this wave vector have flux ratios of up to 0.007 which are strongly correlated with their mean planar kinetic energies. Below we discuss what effect the poorly converged evanescents play in the matching.

In this calculation, we found that using cylindrical rather than spherical cutoffs for the LAPW basis greatly reduced the current densities of the poorly converged states and increased their decay constants. We found that a planar kinetic-energy cutoff of 4 hartrees and a normal kinetic energy cutoff of 4 hartrees were the smallest that produced sufficiently converged states. The best results were achieved using two k_z points symmetric about $k_z=0$ for each parallel wave vector $\mathbf{K}$. A larger sample leads to numerical instabilities in the inversion of the Green matrix, Eq. (13). We found that truncating the basis used in the complex band-structure program by cutting off the number band states computed by the LAPW program made matters worse in all cases and was not used here. There are ways to minimize the impact of such a truncation on the matching, and in cases with larger unit cells the speed-up in computation time will justify a slight loss in accuracy.

B. Twist boundary transmission

We have calculated electron transmission probabilities for scattering from a silicon (111) twist boundary. This

structure, which is shown in Fig. 4, can be constructed by cutting a silicon crystal on a (111) plane through the middle of the bonds perpendicular to that plane, then rotating one half of the crystal 180° around the surface normal, and then reconnecting the crystal so that all cut bonds from one half-crystal are joined with bonds from the other half-crystal. Two adjacent twist boundaries form a stacking fault. This structure is as weak a perturbation of the silicon crystal as is imaginable; no near-neighbor or next-near-neighbor distances have changed, no bonds are broken or even bent, and the cut is in the plane where the potential is weakest. In fact, the potential that results from joining two bulk potentials is continuous because the plane is (screw) symmetric. Along the bonds, where the potential is the strongest, the normal derivative of the potential is also continuous. Thus we should be able to use the joined bulk potentials rather than the self-consistent potential to calculate transmission probabilities without worrying about spurious contributions due to potential discontinuities.

Figure 5 shows the transmission coefficient for conduction-band electron states with zero parallel-wave-vector scattering from the twist boundary described above. Figure 6 shows the transmission coefficient for the states that have the same parallel wave vector as the states at the conduction-band minimum. These states are shown in Figs. 2 and 3 respectively. At energies where more than one propagating transmitted state exists, we sum the magnitude of the transmission probabilities. The transmission calculation is normalized so that unity corresponds to perfect transmission, or zero reflection. A common feature in both plots is that at band extrema the transmission coefficient drops rapidly and in at least some cases goes to zero. We discuss the reason for this drop in greater detail below. The main difference between the two plots is that many of the bands that are used in computing Fig. 5 are degenerate because the Λ line is a symmetry line of the silicon Brillouin zone, while none of the bands that are used in Fig. 6 are. The matching problem

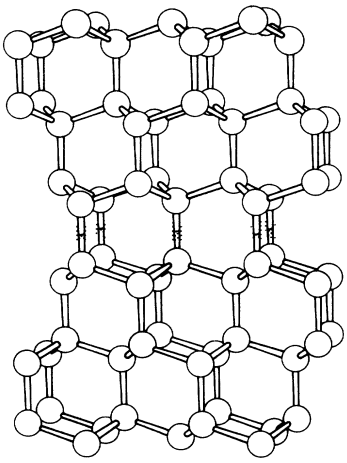

FIG. 4. Ball-and-stick model of a silicon (111) twist boundary. The shaded area in the center of the figure is the matching plane used in the calculation.

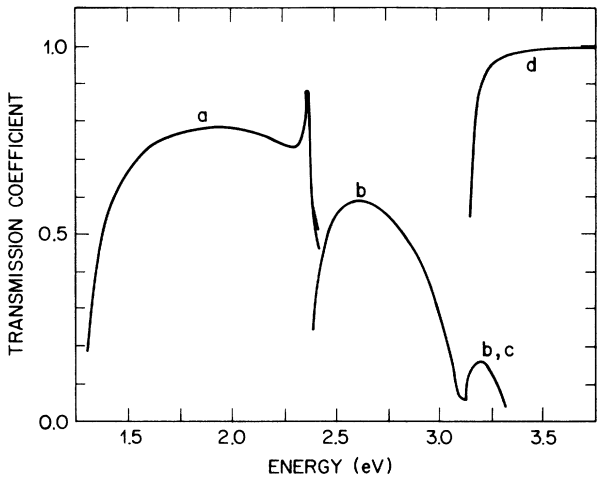

FIG. 5. The transmission coefficient for silicon conduction-band electrons scattering from a (111) twist boundary. Incident-electron states have a parallel wave vector at the $\bar{\Gamma}$ point in the interface Brillouin zone. The transmission coefficient curves are labeled in correspondence with the labels on the dispersion curves of the incident states in Fig. 2. Note that the transmission coefficients for the two parts of the second conduction band (labeled *b* and *c*) are equal. No effort has been made in this plot to precisely explore the behavior of the transmission coefficient near band extrema, where it is usual that the transmission coefficients go to zero.

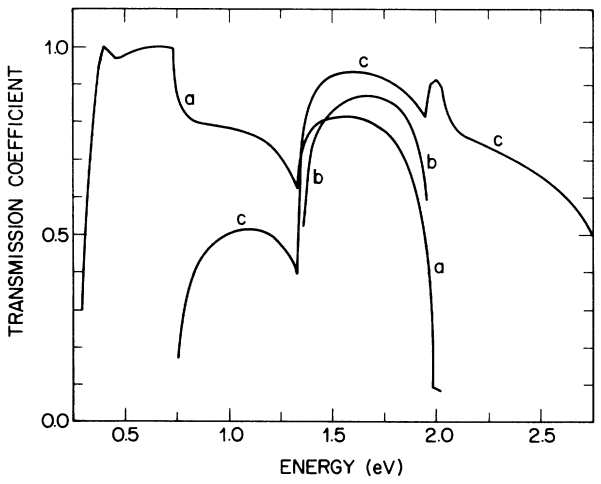

FIG. 6. The transmission coefficient for conduction-band electrons scattering from a (111) twist boundary. Incident-electron states have a parallel wave vector equal to that of an electron at the conduction-band minimum along the Δ line. The transmission coefficient curves are labeled in correspondence with the labels on the dispersion curves of the incident states in Fig. 3. No effort has been made in this plot to precisely explore the behavior of the transmission coefficient near band extrema, where it is usual that the transmission coefficients go to zero (see Fig. 7).

that needs to be solved to construct Fig. 5 breaks into several subproblems, one for each possible symmetry.

Figure 7 shows a detail of the transmission coefficient for the electron states near the minimum of the conduction band. At the band minimum, the transmission coefficient is zero, and it increases linearly and becomes nearly unity until the next band becomes allowed. On the energy scale that is important for devices, within thermal energies of the band minimum, transmission is very poor. This result is contrary to a naive effective-mass-approximation prediction, in which only band discontinuities or changes in effective mass would cause reflection. The breakdown of the naive effective-mass approximation is due to considering only the envelope wave function and neglecting details of the rapidly varying part when matching the wave functions. The avoided crossinglike behavior at 0.5 eV discussed above manifests itself in the small dip in the transmission coefficient in this plot.

Some of the hole states at the valence-band maximum show similar behavior; the transmission coefficients for these states with zero parallel wave vector are shown in Fig. 8. Over a thermal energy range, there is essentially perfect transmission for the split-off holes but poor transmission for the light and heavy holes. The split-off holes behave as is expected in an effective-mass approximation. Again, the difference in behavior is due to the details of the wave functions and their derivatives. Inclusion of spin-orbit coupling will complicate this behavior because these bands are mixed together and shifted in energy, but the decoupling of the different orbital symmetries in the matching will still hold. The split-off hole band will end at a lower energy and will not completely transmit, and there will be some finite transmission for the light and heavy holes at their band maximum.

A more quantitative analysis of the effect of spin-orbit coupling could be achieved by setting up a $\mathbf{k}\cdot\mathbf{p}$ perturbation description of the band structure that fits the LAPW

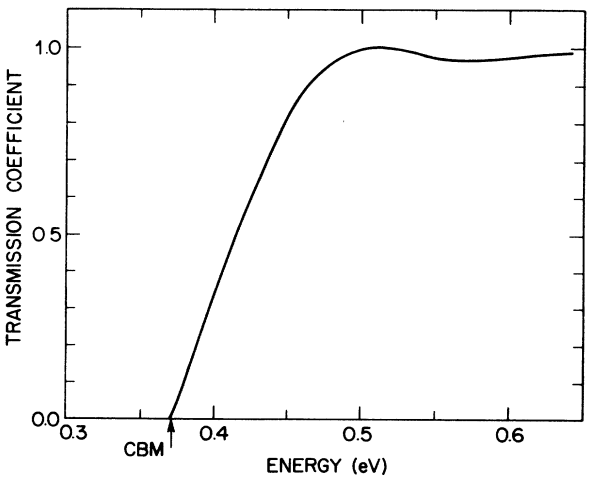

FIG. 7. A detail of the transmission coefficient for electron states near the conduction-band minimum. Over the room-temperature energy range, the electrons are very strongly scattered by the twist boundary.

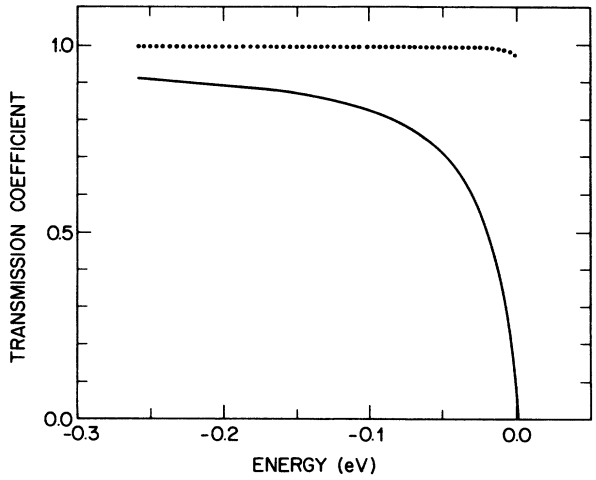

FIG. 8. A detail of the transmission coefficients for hole states near the valence-band maximum. Over the room-temperature energy range, the light- and heavy-hole transmissions (solid curve) show strong scattering by the twist boundary, but the split-off hole transmission (dotted curve) does not.

bands near the valence-band maximum. The mixing of the $\mathbf{k}\cdot\mathbf{p}$ eigenstates by the spin-orbit coupling could then be computed. Since the LAPW bands all have different symmetries, the transmission coefficient for the spin-orbit-split bands would be an average of the transmissions for each of the LAPW bands weighted by the contribution of each nonrelativistic band to the spin-orbit-split band at that wave vector.

Matching the wave functions of the propagating conduction-band states without the inclusion of evanescent states gives the results in Fig. 9. Unlike the previous plots, the net flux in this problem was not constrained to be 1, so we show both the transmission coefficient and the reflection coefficient. Near the band minimum, the transmission is zero for a large range of energies, which implies that the reflected state is a better match for the incident state than the transmitted state is. The top panel of that figure shows the residual of the matching; it is zero at the band minimum, implying that the reflected state is a perfect match for the incident state at that energy. As the energy increases from the minimum, the evanescent states play a more important role and understanding the matching purely in terms of the propagating states becomes impossible.

Matching involves the real and imaginary parts of both the wave functions and their normal derivatives; to understand the states and aspects of the matching process, the probability density and the three flux densities of each state contain the same information, but are real and observable. The probability density and the normal flux density for the three relevant propagating states at an energy close to the conduction-band minimum are shown in Fig. 10.

The probability densities for the state in Fig. 10 are nearly the same, as would be expected near a band minimum. However, the flux density is not simply that of the effective-mass envelope function modulated by

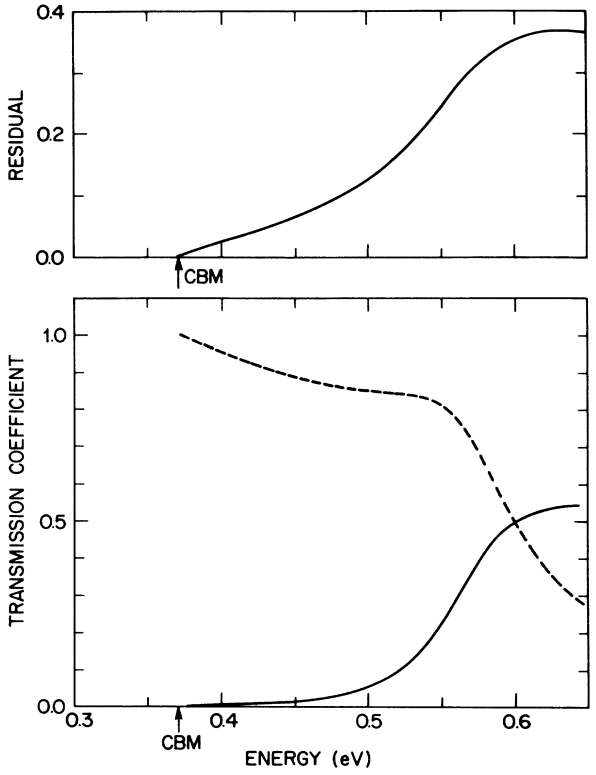

FIG. 9. The transmission coefficient (solid curve) and reflection coefficient (dashed curve) for electron states near the conduction-band minimum computed without evanescent states or flux constraint. The top panel shows the squared residual from the matching. These panels show that perfect reflection at the band minimum results from a perfect match between the incident and reflected states.

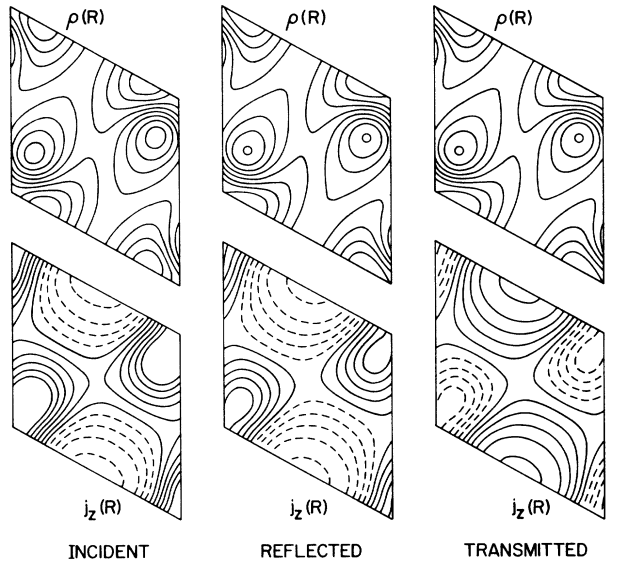

FIG. 10. The probability, ρ, and flux, j_z, densities for states 5.4 meV above the conduction-band minimum. The plotting area is an interface unit cell on the matching plane with the bonds at the corners. Density and flux contours are linearly spaced from 2×10^{-4} to 16×10^{-4} a.u. and -1×10^{-4} to 1×10^{-4} a.u., respectively, dashed contours being negative. The states are normalized to unity over a Wigner-Seitz cell of volume $270a_0^3$. While the probability densities are similar for all three states and the incident flux density is similar to the reflected flux density, it is not similar to the transmitted flux density, leading to the calculated poor transmission.

these probabilities. The band-minimum flux density is not zero, but consists of regions of positive and of negative flux that cancel each other when integrated over the plane. Moving away from the band minimum partially breaks this cancellation, resulting in a net current that is much less than the current in either direction. The flux densities of the incident and the reflected states are similar, while those of the incident state and the transmitted states are nearly opposite. This mismatch, which is contrary to naive effective-mass assumptions, leads to the vanishing band-edge transmission coefficients. The flux mismatch is a nontrivial effect of the 180° rotation. Figure 9 shows that the transmission remains poor, when only the propagating states are included, up to the energy of the band "glitch" discussed above, where one state changes character. What is more difficult to understand in any simple terms is how the evanescents fix up the mismatch, so that the accurately computed transmission, Fig. 7, recovers to unity in ≈ 0.1 eV.

The electrons in the light- and heavy-hole bands shown in Fig. 11 behave the same way, with one additional complication—these two bands are degenerate. It is not enough just to consider the probability density and the normal flux density to reach the same conclusions we

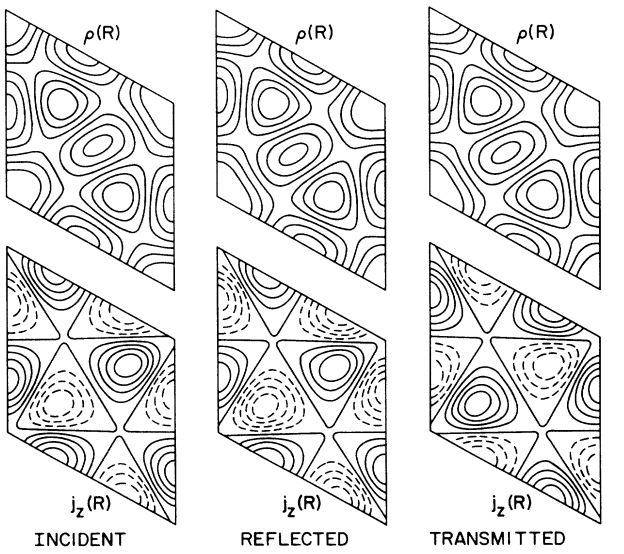

FIG. 11. The probability, ρ, and flux, j_z, densities for light- or heavy-hole states 5.4 meV below the valence-band maximum. Density and flux contours are linearly spaced from 2×10^{-3} to 14×10^{-3} a.u. and -1.6×10^{-4} to 1.6×10^{-4} a.u., respectively, dashed contours being negative.

reached in the previous case. There are transmitted states that match the incident states perfectly with respect to these two quantities, but do not couple at all because they are orthogonal partners of the Λ_2 representation of the small group of the Λ line. This is manifest in their complex phases, which are suppressed in the plotted quantities.

The electrons in the split-off–hole bands shown in Fig. 12 behave differently. The flux densities are roughly proportional to the probability densities, as in a naive effective-mass picture, and do not consist of canceling regions of flux. Thus the transmitted state is a better match for the incident state than the reflected state, and the transmission coefficient is close to 1.

The result that the transmission coefficient goes to zero near band extrema for certain bands should be very general, being intrinsic to the material and probably independent of the details of the interface.

In addition to the transmission coefficient, we have searched for interface states at the two parallel wave vectors we have considered. We found a degenerate pair 0.019 eV above the valence-band maximum at $\bar{\Gamma}$ and one 0.09 eV below the conduction-band minimum at $\bar{\Gamma}$. We found no interface states with a parallel wave vector equal to that of the conduction-band minimum. However, there is a surface resonance at 0.026 eV above the conduction-band minimum. The large reflectivity at band extrema and the existence of interface states and resonances seem to be related. The energies for transmission recovery scale roughly with their energies. One way to view the relationship is that the interface-region density of states lost due to destructive interference between incident and reflected states is compensated for by the interface state. This is borne out by the behavior of the valence states, which have an interface state for the reflected light- and heavy-hole bands, but not for the transmitted split-off–hole band.

The decay constants of the least decaying evanescents at the energies of the interface states we found were quite small, and corresponded to decays in amplitude of 0.85 per layer for the state near the valence band and of 0.65 per layer for the state near the conduction band. It would be extremely difficult to isolate these states in a supercell calculation. In addition, these energies would change significantly if we were calculating the interface-state energies for a stacking fault made of two adjacent twist boundaries or if the atomic positions at the interface were allowed to relax.[37]

The use of constrained least-squares matching makes it easy to monitor the convergence of the results, and, in particular, the effect of the poorly converged "current-carrying" evanescent states in the matching. We found that unconstrained matching with all of the evanescent states leads to an average error of less than 1% in unconstrained total current conservation, which we reduced to less than one-hundredth of a percent by iterating the constraint. Since there were as many outgoing states as parallel wave vectors, the residuals in the unconstrained match were zero, but only increased to the parts-per-million level by imposing the constraint. With or without the constraints, the current of evanescent states, computed by summing magnitude of the current in each separately, was less than one part per thousand. In this case, we found no advantage in discarding the poorly converged evanescents.

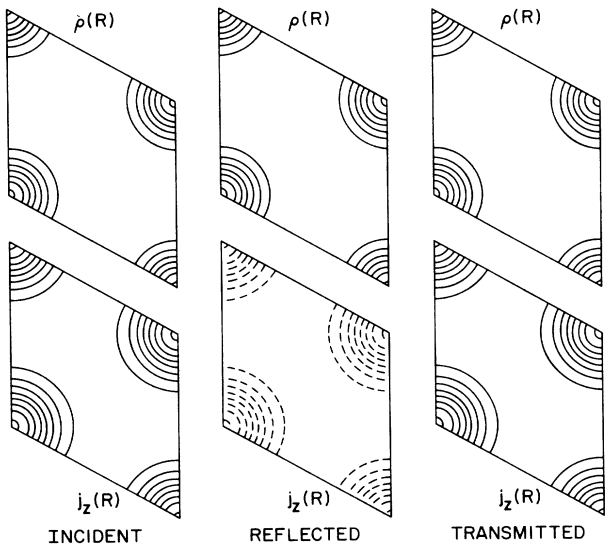

FIG. 12. The probability, ρ, and flux, j_z, densities for split-off–hole states 5.4 meV below the valence-band maximum. Density and flux contours are linearly spaced from 2×10^{-5} to 12×10^{-5} a.u. and -8×10^{-5} to 8×10^{-5} a.u., respectively, dashed contours being negative. The incident flux density is similar to the transmitted flux density and not the reflected flux density, leading to good transmission.

V. CONCLUSIONS

There are two main purposes for this paper, to outline the method we developed and to present some results for electron scattering from a twist boundary.

The method is very powerful and flexible; we are able to calculate the electronic structure of almost any system with two-dimensional periodicity. It is stable because the generalized Bloch states of the system are calculated layer by layer using a variational formalism with a basis set. The matching is done directly at the interface using these states, which allows control of possible errors, and is constrained to force the error away from quantities of interest. By using a joining layer with a self-consistent interface potential that matches the bulk potentials on both its interfaces, potential discontinuities that can lead to spurious results are removed. Our application of this method makes use of an existing electronic-structure program which allows direct interfacing with potentials and matrix elements from that program. That LAPW method uses a basis set that is applicable to any material and to general potentials and simplifies computation dramatically compared to nonlinear methods.

The conclusions from the twist-boundary calculation are twofold: that it is important to do these relatively large calculations because simpler calculations can lead you astray, and that near many band extrema transmis-

sion coefficients go to zero. Only considering the envelope function near these extrema, as is often done in effective-mass approximations, would lead to unreliable predictions. Because the poor transmission is a property of the bulk material, caused by the canceling currents flowing in both directions for some Bloch states at band extrema, it should be a very general effect.

We demonstrated this new method on a relatively simple interface, the silicon twist boundary. Future applications of much greater intrinsic interest will include epitaxial silicon-silicide interfaces, and interfaces between semiconductors, both elemental and compound. Other possible applications might be electron scattering by ordered surfaces and bound states in periodic heterostructures.

ACKNOWLEDGMENT

The authors would like to thank Mark Hybertsen for a critical reading of the manuscript.

APPENDIX

In this appendix we describe the use of the LAPW basis set for variational layer calculations. Such a use is complicated by the different form of the wave function in different parts of space.

We have tried to follow the notation of Ref. 38 as closely as possible; that reference describes the specific implementation of the LAPW method upon which this calculation is based. The LAPW basis function is

$$\psi_i(\mathbf{r})=e^{i\mathbf{k}_i\cdot\mathbf{r}}\Theta^I(\mathbf{r})\frac{1}{\Omega^{1/2}}\sum_{\mathbf{g}}\psi_{\mathbf{g}i}e^{i\mathbf{g}\cdot\mathbf{r}}+\sum_n\Theta^n(\mathbf{r})e^{i\mathbf{k}_i\cdot\mathbf{a}_n}\sum_L\psi^n_{Li}Y_{lm}(\theta,\phi)\phi^n_{l\tau}(|\mathbf{r}-\mathbf{a}_n|)\ . \tag{A1}$$

The interstitial step function, $\Theta^I(\mathbf{r})$, is 1 in the interstitial region and 0 in the muffin tins around each atom. Each muffin-tin step function, $\Theta^n(\mathbf{r})$, is 1 around the nth muffin tin centered at $\mathbf{a}_n$ and 0 elsewhere. In the interstitial region, the wave functions are expanded in plane waves, and in each muffin-tin region they are expanded in spherical harmonics times numerical radial wave functions. By construction, the basis functions are continuous and differentiable across the muffin-tin boundaries up to the highest-angular-momentum component included in the muffin-tin expansion.

The overlap matrix consists of contributions from the interstitial region and each muffin-tin region,

$$O_{ij}=O^I_{ij}+\sum_n O^n_{ij}\ . \tag{A2}$$

We discuss the contribution from the muffin tins below. The contribution from the interstitial region is related to the contribution in the usual LAPW overlap matrix, except that the transformed step function depends on the difference in the z component of the wave vectors as well as the difference in reciprocal-lattice vectors,

$$O^I_{ij}=\sum_{\mathbf{g}}\sum_{\mathbf{g}'}\psi^*_{\mathbf{g}i}\Theta_{\mathbf{g}-\mathbf{g}'}(k_{zi}-k_{zj})\psi_{\mathbf{g}'j}\ . \tag{A3}$$

This situation does not arise in the usual LAPW method, since Bloch functions with different k's integrated over all space are orthogonal. This form of the step function is related to the Fourier transform of the step function,

$$\Theta^I(\mathbf{r})=\sum_{\mathbf{g}}\Theta^I_{\mathbf{g}}e^{i\mathbf{g}\cdot\mathbf{r}}\ , \tag{A4}$$

by

$$\Theta_{\mathbf{g}}(\Delta k_z)=\sum_{g''_z}\Theta^I_{\{\mathbf{G},g''_z\}}\left[\frac{A}{\Omega}\int_{z_L}^{zR}dz\,e^{-i(\Delta k_z+g_z-g''_z)}\right]\ . \tag{A5}$$

The sum over g''_z converges much faster in practice than would be expected by the algebraic falloff in the magnitude of the terms. To evaluate Eq. (A5), it is necessary to compute the Fourier-transformed step function over a much larger set of reciprocal-lattice vectors than is used in the usual LAPW method. The new grid of reciprocal-lattice vectors is long in the direction of the interface normal, which is not, in general, a direction of one of the primitive reciprocal-lattice vectors used in the LAPW program, and requires a new indexing scheme.

The Hamiltonian matrix can also be split into an interstitial contribution and a contribution from each muffin tin,

$$H_{ij}=H^I_{ij}+\sum_n H^n_{ij}\ . \tag{A6}$$

The interstitial contribution is

$$H^I_{ij}=\frac{1}{4m}\sum_{\mathbf{g}}\sum_{\mathbf{g}'}\psi^*_{\mathbf{g}i}(|\mathbf{k}_i+\mathbf{g}|^2+|\mathbf{k}_j+\mathbf{g}'|^2)\Theta_{\mathbf{g}-\mathbf{g}'}(k_{zi}-k_{zj})\psi_{\mathbf{g}'j}+\sum_{\mathbf{g}}\sum_{\mathbf{g}'}\psi^*_{\mathbf{g}i}V^P_{\mathbf{g}-\mathbf{g}'}(k_{zi}-k_{zj})\psi_{\mathbf{g}'j}\ , \tag{A7}$$

using the same transformed step function that is used in the overlap in the symmetrized kinetic-energy term. The potential contribution is related to the overlap contribution in that it involves the projected potential,

$$V^P(\mathbf{r})=\Theta^I(\mathbf{r})V(\mathbf{r})=\sum_{\mathbf{g}}V^P_{\mathbf{g}}e^{i\mathbf{g}\cdot\mathbf{r}}\ , \tag{A8}$$

transformed in the same way as the interstitial step function,

$$V_{\mathbf{g}}^{P}(\Delta k_z)=\sum_{g_z''} V_{\{\mathbf{G},g_z''\}}^{P}\left[\frac{A}{\Omega}\int_{z_L}^{z_R} dx\, e^{-i(\Delta k_z+g_z-g_z'')}\right] . \tag{A9}$$

Computing the Fourier transform of the projected potential requires knowing the Fourier transform of the interstitial step function on yet a larger grid of reciprocal-lattice vectors to do the convolution of the Fourier transform of the unprojected potential and the interstitial step function.

The calculation of the rest of the required quantities depends on whether or not the matching planes cut through any muffin tins. First, we discuss the boundary terms and then the muffin-tin contributions to the overlap and Hamiltonian matrices.

If the matching plane does not cut through any muffin tins, the Fourier transform of the value and slope of the wave functions on the matching planes can be found easily from the expansion of the states in interstitial plane waves. If the matching plane does cut through muffin tins, the Fourier transforms are found by fast Fourier transforms of the wave function or derivative in real space,

$$\psi_{i\mathbf{G}}=\int_{\mathrm{IWSC}} d^2R\, e^{-i\mathbf{K}\cdot\mathbf{R}} e^{-i\mathbf{G}\cdot\mathbf{R}}\psi_i(\mathbf{R},z_X) . \tag{A10}$$

The part of the phase factor due to the normal component of the wave vector, $e^{-i_{zi}z_X}$, is included in the Fourier transform of the state, $\psi_{i\mathbf{G}}$. The real-space values are found from a fast Fourier transform for the interstitial region and by direct evaluation for the muffin tins,

$$\psi_i(\mathbf{R},z_X)=e^{i\mathbf{K}\cdot\mathbf{R}}\sum_{\mathbf{g}} e^{i\mathbf{G}\cdot\mathbf{R}} e^{ig_z z_X}\frac{1}{\Omega^{1/2}}\psi_{\mathbf{g}i}\Theta^{I}(\mathbf{R},z_X) + \sum_n \Theta^n(\mathbf{R},z_X) e^{i\mathbf{K}_i\cdot\mathbf{a}_n}\sum_L \psi_{Li}^n[Y_{lm}(\theta,\phi)\phi_{l\tau}^n(|\mathbf{r}-\mathbf{a}_n|)]\,|_{\mathbf{r}=(\mathbf{R},z_X)} , \tag{A11}$$

$$\partial_z\psi_i(\mathbf{R},z)\,|_{z=z_X}=e^{i\mathbf{K}\cdot\mathbf{R}}\sum_{\mathbf{g}} e^{i\mathbf{G}\cdot\mathbf{R}} e^{ig_z z_X} i(k_z+g_z)\frac{1}{\Omega^{1/2}}\psi_{\mathbf{g}i}\Theta^{I}(\mathbf{R},z_X) + \sum_n \Theta^n(\mathbf{R},z_X) e^{i\mathbf{K}_i\cdot\mathbf{a}_n}\sum_L \psi_{Li}^n\{\hat{\mathbf{z}}\cdot\nabla[Y_{lm}(\theta,\phi)\phi_{l\tau}^n(|\mathbf{r}-\mathbf{a}_n|)]\}\,|_{\mathbf{r}=(\mathbf{R},z_X)} . \tag{A12}$$

The gradient in radial coordinates is evaluated using the expression

$$\begin{aligned}\nabla[Y_{lm}(\theta,\phi)f(r)]=\hat{\mathbf{r}}\frac{df(r)}{dr}Y_{lm}(\theta,\phi)+\hat{\theta}\frac{f(r)}{2r}[&(l+m+1)^{1/2}(l-m)^{1/2}Y_{l,m+1}(\theta,\phi)e^{-i\phi}\\ &-(l-m+1)^{1/2}(l+m)^{1/2}Y_{l,m-1}(\theta,\phi)e^{i\phi}]\\ +\hat{\phi}\frac{if(r)}{2r}\{&2m\sin\theta Y_{lm}(\theta,\phi)-\cos\theta[(l+m+1)^{1/2}(l-m)^{1/2}Y_{l,m+1}(\theta,\phi)e^{-i\phi}\\ &+(l-m+1)^{1/2}(l+m)^{1/2}Y_{l,m-1}(\theta,\phi)e^{i\phi}]\} ,\end{aligned} \tag{A13}$$

which requires no potentially unstable divisions and uses stable recursion relations for the derivatives of Legendre polynomials.

If the matching planes do not intersect any muffin tins, the overlap and Hamiltonian matrix elements are straightforward to calculate. The overlap matrix

$$O_{ij}^n=\sum_L\sum_{L'}\psi_{Li}^{n*}\Theta_{L,L'}^n\psi_{L'j}^n \tag{A14}$$

is given in terms of a diagonal matrix of the normalizations of the radial functions since the wave-vector dependence of the state is absorbed into the matching coefficients on the muffin-tin spheres,

$$\Theta_{L,L'}^n=e^{-i(\mathbf{k}_i-\mathbf{k}_j)\cdot\mathbf{a}_n}\omega_{l\tau}\delta_{L,L'} . \tag{A15}$$

The Hamiltonian matrix,

$$H_{ij}^n=\sum_L\sum_{L'}\psi_{Li}^{n*}\tilde{H}_{L,L'}^{n}\psi_{L'j}^n , \tag{A16}$$

is given in terms of the Hamiltonian matrix already used in the LAPW program scaled by a phase factor,

$$\tilde{H}_{L,L'}^{n}=e^{-i(\mathbf{k}_i-\mathbf{k}_j)\cdot\mathbf{a}_n}H_{L,L'}^n . \tag{A17}$$

These expressions are valid for any muffin tins that are not cut by the matching plane even if some others are.

If one of the matching planes does cut through a muffin tin, and the layer contains an entire unit cell as used in the LAPW program, there will be a contribution from each section of the muffin tin with a different phase,

$$\Theta_{L,L'}^n=e^{-i(\mathbf{k}_i-\mathbf{k}_j)\cdot\mathbf{b}_{nR}}\Theta_{L,L'}^{nR}+e^{-i(\mathbf{k}_i-\mathbf{k}_j)\cdot\mathbf{b}_{nL}}\Theta_{L,L'}^{nL} . \tag{A18}$$

The muffin-tin centers $\mathbf{b}_{nX}$ are those that place the appropriate part of the muffin tin in the layer under consideration. If the two wave vectors are the same, the left- and right-hand contributions add to become the diagonal form given in Eq. (A15). If the layer under consideration is a partial layer, the contribution from the left, right, or both may be zero because that piece is outside the layer. The step function for a partial sphere is

$$\Theta^{nR}_{L,L'}=\sum_{l''m''}\int d\Omega[Y^*_{lm}(\theta,\phi)Y_{l'm'}(\theta,\phi)Y_{l''m''}(\theta,\phi)]R^{l''}_{m''0}(\hat{\mathbf{z}},\hat{\mathbf{u}})\int_0^{r_n} dr\, r^2\phi^n_{l\tau}(r)\phi^n_{l'\tau'}(r)\Theta^u_{l''}(r)\ , \tag{A19}$$

which consists of three factors. There is a Gaunt coefficient of the two angular-momentum states and the spherical harmonic from the expansion of the cut muffin-tin step function. A rotation matrix, R, aligns the direction with which the spherical harmonics are defined, $\hat{\mathbf{u}}$, with the interface normal, $\hat{\mathbf{z}}$. Finally there is the integral of the two radial functions and the radial part of the cut muffin-tin step function Θ^u. The radial part of the step function is given by an integral over the angular coordinate of a step function that depends both on the angular coordinate and the radius,

$$\Theta^u_l(r)=\int_{-1}^{1}d\mu\left[\frac{2l+1}{4\pi}\right]^{1/2}P_l(\mu)\Theta\left[\mu-\frac{z^n_R}{r}\right]\ , \tag{A20}$$

where z^n_R is the signed distance from the muffin-tin center to the closest approach of the matching plane. This integration can be evaluated by an indefinite integral for the Legendre polynomials,

$$l\int^{\mu}d\mu' P_l(\mu')=P_{l+1}(\mu)-\mu P_l(\mu)\ . \tag{A21}$$

If $r<-z^n_R$ this expression reduces to $(4\pi)^{-1/2}\delta_{l,0}$. Similar expressions to these hold for the contributions from the left-hand sections of each muffin tin.

The Hamiltonian matrix is also split up into contributions from both parts of a muffin tin that is cut,

$$\tilde{H}^{\ n}_{L,L'}=e^{-i(\mathbf{k}_i-\mathbf{k}_j)\cdot\mathbf{b}_{nR}}\tilde{H}^{\ nR}_{L,L'}+e^{-i(\mathbf{k}_i-\mathbf{k}_j)\cdot\mathbf{b}_{nL}}\tilde{H}^{\ nL}_{L,L'}\ . \tag{A22}$$

For each section there is a contribution from the kinetic energy and the spherically averaged potential, and a contribution from the nonspherical parts of the potential,

$$\tilde{H}^{\ nR}_{L,L'}=\frac{\epsilon^n_l+\epsilon^n_{l'}}{2}\Theta^{nR}_{L,L'}+\tfrac{1}{2}\delta_{\tau,2}\Theta^{nR}_{lm\tau-1,L'}+\tfrac{1}{2}\delta_{\tau',2}\Theta^{nR}_{L,l'm'\tau'-1}+V^{nR}_{L,L'}\ . \tag{A23}$$

The first contribution is proportional to the muffin-tin step function discussed above the symmetrized radial eigenvalues. The second and third terms in Eq. (A23) arise because the energy-derivative radial functions satisfy an inhomogeneous Schrödinger equation. The contribution from the nonspherical parts of the potential can be cast in a form similar to that for the cut muffin-tin step function,

$$V^{nR}_{L,L'}=\sum_{l'',m''}\int d\Omega[Y^*_{lm}(\theta,\phi)Y_{l'm'}(\theta,\phi)Y_{l''m''}(\theta,\phi)]\int_0^{r_n}dr\, r^2\phi^n_{l\tau}(r)\phi^n_{l'\tau'}(r)\tilde{V}^{\ n}_{l''m''}(r)\ , \tag{A24}$$

in which the radial part of the cut muffin-tin potential has replaced the radial part of the cut muffin-tin step function. The radial part of the cut muffin-tin potential can be calculated in terms of Gaunt coefficients, the uncut radial parts of the potential, and the radial part of the cut muffin-tin step function,

$$\tilde{V}^{\ n}_{lm}(r)=\sum_{\substack{l'>0\\ m'}}\sum_{l''}V^n_{l'm'}(r)\Theta^u_{l''}(r)\left[\sum_{m''}\int d\Omega[Y^*_{lm}(\theta,\phi)Y_{l'm'}(\theta,\phi)Y_{l''m''}(\theta,\phi)]R^{l''}_{m''0}(\hat{\mathbf{z}},\hat{\mathbf{u}})\right]\ . \tag{A25}$$

The cut muffin-tin potential is stored in a symmetrized fashion similar to the storage of the full muffin-tin potential in the existing LAPW program,[38] except with reduced symmetry due to the cutting plane. In principle, the cut potential must be calculated for all l's up to twice the cutoff used for the wave functions, but, in practice, this is not necessary. The l'' sum runs from zero to the l cutoff used for the full muffin-tin potential plus that used for the cut muffin-tin potential.

[1]*Proceedings of the 18th International Conference on the Physics of Semiconductors, Stockholm, 1986,* edited by O. Engström (World Scientific, Singapore, 1987).

[2]E. Rosencher, S. Delage, Y. Campidelli, and F. Arnaud d'Avitaya, Electron. Lett. **20**, 726 (1984); J. C. Hensel, A. F. Levi, R. T. Tung, and J. M. Gibson, Appl. Phys. Lett. **47**, 151 (1985).

[3]H. Bross, J. Phys. F **12**, 2883 (1982).

[4]G. Wachutka, Phys. Rev. B **34**, 8512 (1986).

[5]J. A. Applebaum and D. R. Hamann, Solid State Commun. **27**,

881 (1978); J. A. Applebaum and D. R. Hamann, Rev. Mod. Phys. **48**, 479 (1976).

[6]D. Spanjaard, D. W. Jepsen, and P. M. Marcus, Phys. Rev. B **19**, 642 (1979).

[7]R. Hora and M. Scheffler, Phys. Rev. B **29**, 692 (1984).

[8]J. B. Pendry, Surf. Sci. **57**, 679 (1976).

[9]M. Seel, Phys. Rev. B **28**, 2268 (1983).

[10]G. Bastard, Phys. Rev. B **24**, 5693 (1981).

[11]G. C. Osbourn and D. L. Smith, Phys. Rev. B **19**, 2124 (1979).

[12]S. R. White and L. J. Sham, Phys. Rev. Lett. **47**, 879 (1981); S. R. White, G. E. Margues, and L. J. Sham, J. Vac. Sci. Technol. **21**, 544 (1982).

[13]A. C. Marsh and J. C. Inkson, J. Phys. C **19**, 43 (1986); A. C. Marsh and J. C. Inkson, *ibid.* **17**, 6561 (1986); A. C. Marsh and J. C. Inkson, Solid State Commun. **52**, 1037 (1984).

[14]Y.-C. Chang and J. N. Schulman, J. Vac. Sci. Technol. **21**, 540 (1982).

[15]M. G. Burt and J. C. Inkson, J. Phys. D **9**, 43 (1976).

[16]P. Dzwig, M. G. Burt, J. C. Inkson and V. Crum, J. Phys. C **15**, 1187 (1982).

[17]F. Garcia-Moliner and F. Flores, *Introduction to the Theory of Solid Surfaces* (Cambridge University Press, Cambridge, 1980).

[18]K. Kambe, Z. Naturforsch. **22a**, 322 (1967); **22a**, 422 (1967); K. Kambe, *ibid.* **23a**, 1280 (1968); K. Kambe, Surf. Sci. **117**, 443 (1982).

[19]E. Molinari, G. B. Bachelet, and M. Altarelli, Surf. Sci. **152/153**, 1178 (1985); E. Molinari, G. B. Bachelet, and M. Altarelli, J. Phys. (Paris) Colloq. **46**, C4-321 (1985).

[20]G. Wachutka and H. Bross, J. Phys. A **15**, 3083 (1982).

[21]Even though we use atomic units in which $m=1$, we include m in equations to differentiate between those quantities that have units of energy, 1 hartree$=27.2$ eV, and those that have units of inverse length squared, a_0^{-2}, where a_0 is the Bohr radius. In atomic units (1 hartree)$ma_0^2=1$.

[22]The spectral representation of the Green function in linear-combination-of-atomic-orbitals (LCAO) -based methods is well behaved in the joining equations if volume integrals of overlapping basis functions rather than value and slope matching are used to determine the eigenstates of a composite system. Defects in semiconductors have been studied using such calculations. See, for example, G. A. Baraff and M. Schlüter, Phys. Rev. B **30**, 1853 (1984).

[23]See, for example, W. H. Press, B. P. Flannery, S. A. Teukolsky, and W. T. Vetterling, *Numerical Recipes* (Cambridge University Press, Cambridge, 1986).

[24]See, for example, G. Strang and G. Fix, *An Analysis of the Finite Element Method* (Prentice-Hall, Englewood Cliffs, NJ, 1973).

[25]O. K. Andersen, Phys. Rev. B **12**, 3060 (1975).

[26]Y.-C. Chang and J. N. Schulman, Phys. Rev. B **25**, 3975 (1982).

[27]C. Mailhoit, D. L. Smith, and T. C. McGill, J. Vac. Sci. Technol. B **1**, 3 (1983); **1**, 637 (1983).

[28]E. O. Kane J. Phys. Chem. Solids **1**, 249 (1957).

[29]J. Inglesfield, J. Phys. C **4**, L14 (1971); G. A. Benesh and J. E. Inglesfield, *ibid.* **17**, 1595 (1984).

[30]J. B. Pendry, *Low Energy Electron Diffraction* (Academic, London, 1974).

[31]R. W. Godby, M. Schlüter and L. J. Sham, Phys. Rev. Lett. **56**, 2415 (1986); **35**, 4170 (1987).

[32]M. S. Hybertsen and S. G. Louie, Phys. Rev. Lett. **55**, 1418 (1985); Phys. Rev. B **34**, 5390 (1986).

[33]Errors in band-gap lineup due to the local-density approximation can be treated empirically by adding a smooth "lineup" potential through the joining layer if necessary.

[34]L. C. Kaufman, ACM Trans. Math. Software **1**, 271 (1975).

[35]C. Herring, Phys. Rev. **52**, 365 (1937).

[36]W. Kohn, Phys. Rev. **115**, 809 (1959).

[37]M. Y. Chou, S. G. Louie, and M. L. Cohen, in *Proceedings of the 17th International Conference on the Physics of Semiconductors,* edited by J. D. Chadi and W. A. Harrison (Springer-Verlag, New York, 1985), p. 43.

[38]L. F. Mattheis and D. R. Hamann, Phys. Rev. B **33**, 823 (1986).

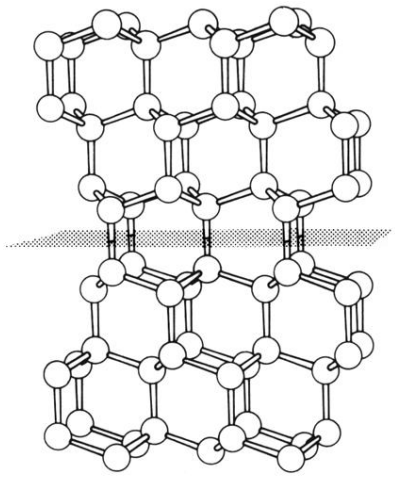

FIG. 4. Ball-and-stick model of a silicon (111) twist boundary. The shaded area in the center of the figure is the matching plane used in the calculation.